

## A 10 Megahertz Spatial Light Modulator

Xin Wei,<sup>1,\*</sup> Zeyang Li,<sup>1,2,\*</sup> Abhishek V. Karve,<sup>1</sup> Adam L. Shaw,<sup>1,2</sup> David I. Schuster,<sup>1</sup> and Jonathan Simon<sup>1,2,†</sup>

<sup>1</sup>*Department of Applied Physics, Stanford University, Stanford, CA*

<sup>2</sup>*Department of Physics, Stanford University, Stanford, CA*

(Dated: January 15, 2026)

Rapid and programmable shaping of light fields is central to modern microscopy [1–3], display technologies, optical communications and sensing [4–6], quantum engineering [7–14], and quantum information processing [15–24]. Current wavefront shaping technologies face a fundamental dichotomy: spatial light modulators (SLMs) offer high pixel count but suffer from low refresh rates, while acousto-optic deflectors (AODs) provide moderate speed with restricted optical beam geometries [25, 26]. Though recent advances in photonic integrated circuits achieve fast switching [27], there is currently no tool that provides MHz-rate, continuous motion, and arbitrarily reconfigurable control over a set of diffraction-limited spots. Here we introduce a new class of spatial light modulator that provides both 2D pixel geometry and high speed. The device operates by encoding spatial information in frequency bins via a broadband optical phase modulator, and decoding them via a first-of-its-kind, high-resolution 2D spectrometer. The spectrometer, based on the architecture which we call the Re-Imaging Phased Array (RIPA), achieves its sensitivity through long path-lengths, enabled by intra-spectrometer re-imaging lens-guides. We demonstrate site-resolved optical pulsing with a 44(1) ns rise time, corresponding to frame rates exceeding 10 million frames per second, as well as arbitrary, reconfigurable 2D addressing and multi-site operations, including asynchronous, independent beam motion, splitting, and recombination. Leveraging these tools opens new horizons in rapid optical manipulation of matter across science, from fast, scalable control that approaches the inertial and radiation limits of atoms in quantum processors, to dynamically programmable, microsecond-resolved illumination in microscopy and neuro-biological imaging [28, 29].

High-speed spatial light modulation enables diverse applications across disparate length scales and technical fields, from macroscopic 3D optical metrology [4], to microscopic wave engineering for high-contrast imaging [1–3], as well as optically multiplexed communication [5, 6]. In atomic, molecular and optical physics, it enables dynamically switchable optical traps [7–9], tunable coupling strength in quantum optical systems [10], global and local modulation in quantum gases [8, 11], and arbitrary excitation in multi-mode cavity quantum electrodynamics [12–14].

For neutral-atom quantum computers in particular, high speed local addressing tools are critical for parallelized atom control. Increasing the speed of these operations while ensuring they remain independently actuated has the potential to accelerate numerous computing primitives, from faster *in-situ* gate operations [15, 16], to independent atom movement [17–19] which enables continuous atom reloading in the processor [20–22], and, perhaps most importantly, the more efficient execution of quantum algorithms [30] by relaxing the co-design/transversal-block-gate requirements [23, 24, 31, 32] necessary for high-rate computation.

Existing local addressing solutions offer either high pixel count or high frame rate, but not both: Digital micromirror devices (DMDs) and conventional spatial light modulators (SLMs) both offer 2D image generation but are limited to  $\sim$  kilohertz frame rates by their

physics: either mirror inertia or the liquid-crystal response time. Combining a DMD and a SLM has recently demonstrated large-scale 2D modulation at frame rates up to 43 kHz [33], which alleviates challenges in local gates, but is insufficient for independent atom transport. Crossed acousto-optic deflectors (AODs) provide near-microsecond switching and beam steering, yet intrinsically generate either a single spot, or a grid of spots (an outer product of one-dimensional patterns) [25, 26], limiting independent addressing capabilities. Furthermore, AOD response times are limited by the acoustic propagation time across the beam waist, hindering rapid dynamical control [17, 34, 35]. A recent approach based on integrated electro-optics delivers impressive bandwidths [27], but has yet to be demonstrated at scale.

We introduce a high-bandwidth spatial light modulation architecture that fundamentally departs from these conventional technologies. Unlike traditional methods that rely on piecing together many low-bandwidth modulators (e.g., acousto-optic, electro-optic, liquid-crystal, MEMS) and stacking parallel control lines to increase aggregate bandwidth, we densely encode spatial information in the frequency domain. This approach allows us to directly harness the 10's of GHz bandwidth of commercial waveguide electro-optical modulators (EOMs). Converting these frequency components to spatial locations necessitates a dispersive element with exceptionally high spectral resolution, but conventional dispersive devices face intrinsic limitations: diffraction gratings are limited by physical beam size, while Virtually Imaged Phased Arrays (VIPAs) [36–38]—which enhance spectral dispersion by circulating the beam within an etalon—suffer from

\* These authors contributed equally.

† [jonsimon@stanford.edu](mailto:jonsimon@stanford.edu)

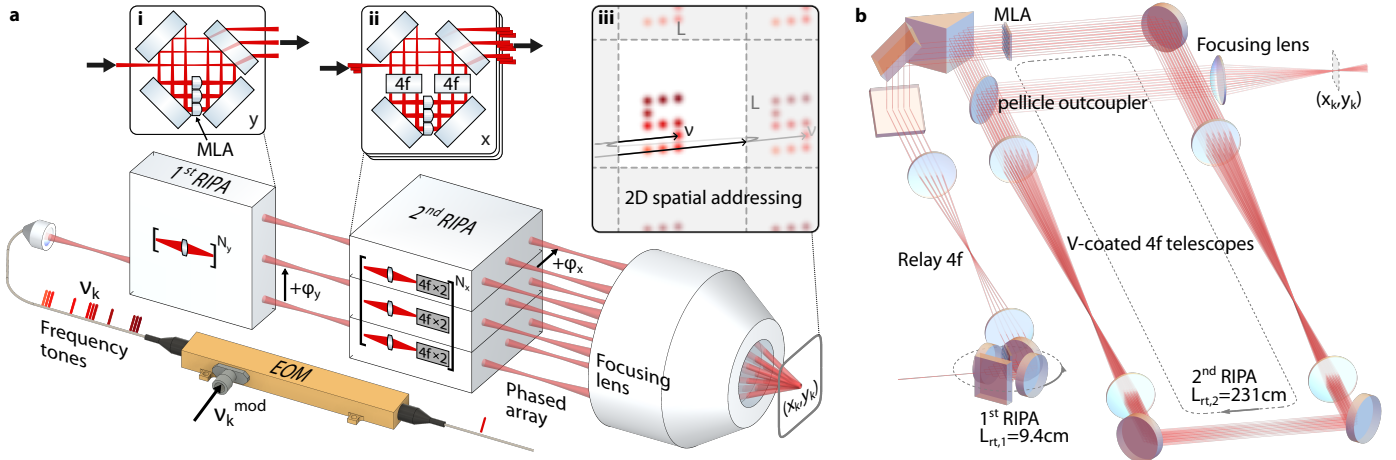


**FIG. 1. Operation of a 10 Mega-FPS spatial light modulator.** **a**, We introduce the Re-Imaging Phased Array (RIPA), a device that enables a first-of-its-kind highly-dispersive, two-dimensional spectrometer for high-bandwidth spatial addressing using controlled frequency multiplexing. An input beam is converted into a 2D beam array by the first and second RIPAs (insets **i** and **ii**). Each RIPA duplicates and displaces the beam over each round trip, during which the beams acquire relative propagation phases  $\varphi_y(\varphi_x)$ , determined by the round-trip path lengths of the first (second) RIPA and the laser frequency. Beam diffraction over the long round trips is suppressed by refocusing optics, yielding a uniform transverse mode across the 2D phased array. Interfering these beams with a focusing lens performs frequency-to-position mapping. When the coherent input beam is phase-modulated by a high-bandwidth electro-optic modulator (EOM) to generate designed frequency tones  $\nu_k$  (shades of red after EOM), the RIPA-spectrometer directs each tone to a specific location  $(x_k, y_k)$ . Increasing the frequency rasters the spot through the Brillouin zone, wrapping around at the edge. Programmable RF modulation therefore synthesizes arbitrary 2D images at the spectrometer output (inset **iii**). **b**, Detailed optical layout of the RIPA system. Diffraction-less propagation is accomplished using a running-wave pseudo-cavity geometry with: an intra-path microlens array (MLA) in the first RIPA, and an identical MLA + two 4f telescopes in the second RIPA (to add propagation distance without spatial inversion).

diffractive beam expansion that degrades spatial mode overlap. Similarly, optical cavities offer high dispersion but only spatially resolve a single output frequency.

Motivated by these considerations, we demonstrate a self-imaging VIPA, which we call a Re-Imaging Phased Array (RIPA), that enables a high-speed optical display via programmable, frequency-encoded modulation. The RIPA architecture integrates a folded, unit-magnification self-imaging relay with a microlens array (MLA), providing a device featuring robust spatial mode with megahertz-level frequency resolution. It provides update rates exceeding 10 MHz, two orders of magnitude faster than the widely used approach based on AODs or the recent combined DMD-SLM method [33]. In what follows, we first outline the operating principle of the device, then characterize a simplified 1D spectrometer, extend it to 2D to demonstrate arbitrary pattern generation, and quantify its performance. Finally, we demonstrate sub-microsecond operation, directly confirming its ability to perform high-speed, multiplexed site addressing.

## PRINCIPLE OF OPERATION

The RIPA architecture generates a phased output beam array with large inter-beam optical path differences, whilst maintaining a uniform spatial profile across all beams. This ensures a large-scale and sta-

ble frequency-to-phase mapping, enabling the array to be focused to a frequency-controlled position with a high-quality interference spot.

We first give a high level summary of the device, with more details provided below. As shown in Fig. 1a, an input beam traverses the first RIPA (inset **i**) and subsequently the second RIPA (inset **ii**) oriented along the orthogonal axis, generating a collimated  $N_x \times N_y$  beam array in which each beam, corresponding to a single microlens pupil, shares a well-defined, common spatial mode. After passing through both RIPAs, the  $(i, j)$ -th beam in the array acquires a cumulative phase shift  $\varphi_{i,j} = i\varphi_x + j\varphi_y$ , where  $\varphi_x$  ( $\varphi_y$ ) represents the round-trip phase accrued within the second (first) RIPA. Focusing this phased array maps input laser frequencies  $\nu_k$  to individual spots  $(x_k, y_k)$  (inset **iii**), and different frequency components can be modulated ( $\nu_k^{\text{mod}}$ ) and swept simultaneously and independently. The number of round trips through the device ( $N_x$  and  $N_y$ ) determines the number of resolvable spots  $N_{\text{res}} = N_x N_y$  in the focal plane. In this work, the first and second RIPAs have round-trip lengths of  $L_{\text{rt},1} = 9.4$  cm and  $L_{\text{rt},2} = 231$  cm, respectively (drawn to scale in Fig. 1b).

We now present a detailed description of the apparatus. The first RIPA generates a 1D phased beam array with a common spatial mode shared by all beams at its output. As shown in Fig. 1a, a single Gaussian beam enters and circulates within the first RIPA repeatedly (inset

i). We introduce an intra-RIPA microlens array (MLA) that functions analogously to the curved mirrors or lenses in an optical cavity [39, 40], maintaining a stable optical mode by periodically refocusing the beam and stabilizing its trajectory against perturbations from slowly varying optical aberrations. Unlike a standard cavity where the beam path closes after a round trip, in the RIPA, the four mirrors fold the beam path and enforce a net transverse displacement of the beam in the  $y$ -direction on each round-trip, matching the MLA pitch of  $p = 1\text{mm}$ . The microlenses situated in the beam path form a lens-guide that re-imagines the beam onto itself (up to the round-trip displacement), ensuring transverse spatial-mode stability over multiple round trips, so long as the input beam is mode-matched to the eigenmode of the lens-guide. We operate near the “half confocal” regime of the lens-guide, where the Gouy phase per pass is  $\pi/4$ , and the mode waist is  $w_0 = \sqrt{f_{\text{MLA}}\lambda/\pi} \sim 108\text{ }\mu\text{m}$ , providing maximum robustness against mode mismatch and aberrations while minimizing clipping loss at MLA pupils (see Methods).

We cascade this process along the orthogonal ( $x$ ) direction through a rotated periscope to form a two-dimensional phased array using a second RIPA (inset ii) with a much higher frequency sensitivity. This RIPA is constructed by adding two 4f unit-magnification telescopes in addition to the first RIPA geometry, which extends the round-trip length to  $L_{\text{rt},2} = 2 \cdot L_{4\text{f}} + L_{\text{rt},1}$ . The telescopes together with folded round trips extends the total optical path length  $N_x L_{\text{rt},2}$  to tens of meters, yielding a frequency resolution of  $f_{\text{res}} = c/(N_x L_{\text{rt},2}) = 16\text{ MHz}$  which also sets the modulation bandwidth of RIPA spatial light modulator. The round-trip propagation matrices of the two RIPAs are identical (but not unity), such that the output of the first RIPA is mode-matched for injection into the second RIPA.

Sequential propagation through the first and second RIPA results in a 2D phased array with a phase profile of  $i\varphi_x + j\varphi_y$  for the  $(i, j)$ -th output beam, where  $\varphi_y$  ( $\varphi_x$ ) is the acquired phase during propagation in the first (second) RIPA round trip, which also sets the relative phase between adjacent beams in the phased array. To interfere the beams (and thus generate a frequency-dependent localized spot), the phased array is focused through a lens (focal length  $f$ ) into an image plane (inset iii): here the beams interfere to form a periodic 2D grid of many Brillouin zones (in analogy with band structures in solid-state physics) whose periodicity is given by  $L = \frac{f\lambda}{p}$  (see Methods), and whose displacement in the focal plane is set by the relative phases  $\varphi_{x,y}$ , and thus the laser frequency  $\nu$ . Within the first Brillouin zone (of area  $L \times L$  in the focal plane), each laser frequency maps to an interference spot at  $(x, y) = (L\frac{\varphi_x}{2\pi}, L\frac{\varphi_y}{2\pi})$ , where  $\varphi_{x,y} \in [-\pi, \pi]$ . Moving forward, we will consider only this first Brillouin zone.

The phases  $\varphi_{x,y}$  evolve linearly with the laser frequency  $\nu$  proportional to the round-trip path lengths of the corresponding RIPAs:  $\Delta\varphi_x = \frac{2\pi L_{\text{rt},2}}{c} \Delta\nu$  and

$\Delta\varphi_y = \frac{2\pi L_{\text{rt},1}}{c} \Delta\nu$ , respectively. By designing the RIPAs with a large path-length ratio ( $L_{\text{rt},2} \gg L_{\text{rt},1}$ ), we establish a separation of scales in the phase evolution: As the laser frequency  $\nu$  is swept, the phase  $\varphi_x$  wraps through the full  $2\pi$  range  $R = L_{\text{rt},2}/L_{\text{rt},1}$  times before  $\varphi_y$  completes a single  $2\pi$  cycle. Consequently, a frequency ramp repeatedly rasters the output point across the  $x$ -axis, with a slower shift along the  $y$ -axis. The full frequency spectrum is thus folded into the 2D spatial domain, filling the Brillouin zone row-by-row (see Fig. 1a iii), reminiscent of a cathode ray tube’s (CRT) raster pattern.

By simultaneously injecting multiple optical tones at frequencies  $\{\nu_k\}$  into the cascaded RIPAs, the output forms a sum of phased arrays with different characteristic phases  $\{(\varphi_{x,k}, \varphi_{y,k})\}$ ; the focused pattern thus simultaneously addresses multiple locations  $\{(x_k, y_k)\}$  within the first Brillouin zone of the image plane. Generating these tones via high-bandwidth electro-optic modulation allows independent amplitude control to produce arbitrary intensity patterns (inset iii).

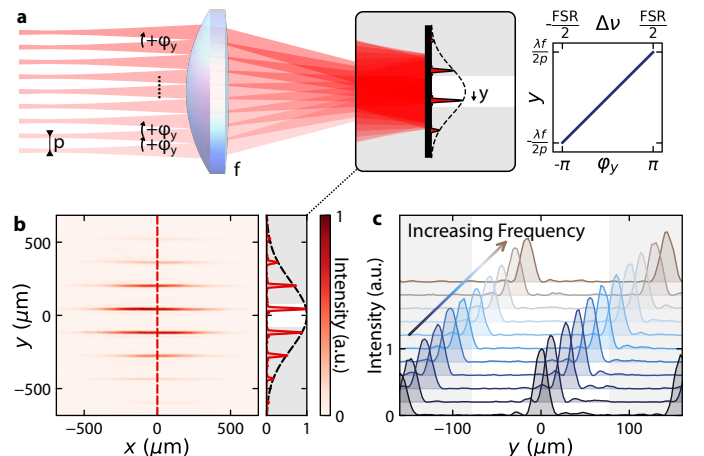


**FIG. 2. 1D phased-array frequency-to-position mapping.** For a single frequency input, a 1D RIPA produces, at its output a, an array of parallel beams with pitch  $p$  and a controllable phase step between adjacent beams  $\varphi_y$ . A lens with focal length  $f$  interferes these beams to produce a focused intensity pattern whose envelope (dashed curve) is set by the single-beam size and whose peak position  $y$  is set by  $\varphi_y$ . The insets illustrate the expected linear relationship between optical frequency detuning  $\Delta\nu$  (modulo one free spectral range, FSR) and output position  $y$ , within the first Brillouin zone (unshaded) spanning  $\pm\lambda f/2p$ . b, Measured focal-plane intensity distribution for a single-frequency input. The dashed vertical line indicates the line-cut shown to the right, where the red curve is the measured line-cut profile and the dashed black curve is the Gaussian envelope corresponding to a single beam in the phased array. c, Intensity profiles along the line-cut in b for increasing laser frequency, showing continuous peak translation across the image plane consistent with the designed frequency-to-position mapping.

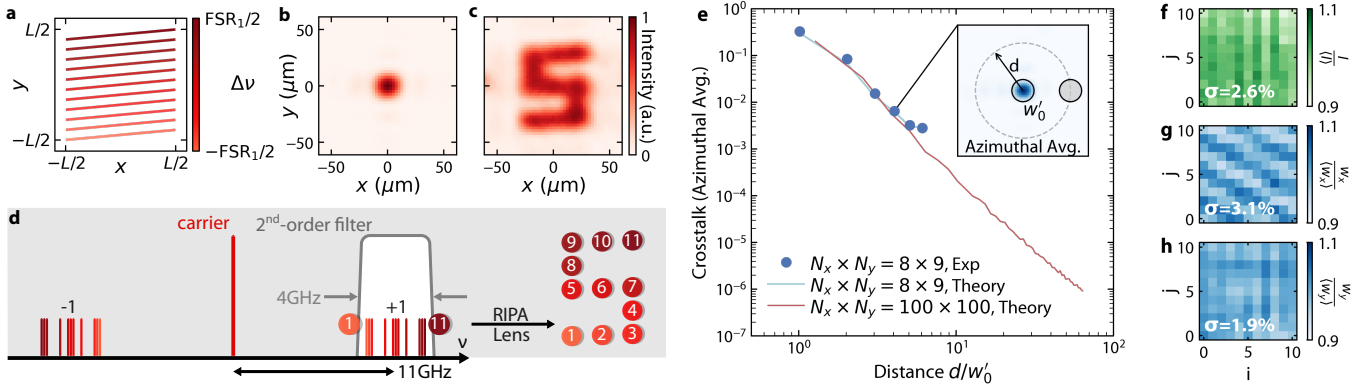


**FIG. 3. Spectrally programmed 2D image synthesis and static characterization.** **a**, Principle of 2D frequency-to-position mapping: Sweeping the laser frequency  $\nu$  (color scale) drives the addressing spot along a tilted raster trajectory across the Brillouin zone row-by-row. **b**, Injection of a single optical tone generates a (measured) intensity distribution corresponding to a diffraction-limited spot. **c**, Synthesis of an "S"-shaped pattern via simultaneous injection of multiple optical tones. **d**, Frequency-domain synthesis of the pattern in **c**. The pattern can be decomposed into 11 independent spots, each corresponding to a unique optical frequency  $\nu_k$  that the RIPA+lens system maps to a distinct spatial location. This optical spectrum is generated by RF driving of a high-bandwidth electro-optic phase modulator, which in practice produces symmetric optical sidebands on the input light, and leaves a strong carrier - a custom, second-order flat-top optical filter [41] transmits only the  $+1$  order blue sidebands, suppressing all other orders and the carrier. **e**, The crosstalk in this system comes directly from the discreteness of the phased array, resulting in power-law tails on each spot. Here we plot the measured (blue circles) and predicted (blue curve) crosstalk between two addressed sites as a function of their separation  $d$ , in units of the  $1/e^2$  intensity radius  $w'_0$ . Scaling to a  $100 \times 100$  array (red curve) predicts crosstalk levels below  $10^{-4}$  at moderate separations. **Inset**: Crosstalk is calculated through azimuthal averaging (along the dashed circle) the integrated intensity within one beam waist radius (solid circle). **f-h** System-wide uniformity maps across the first Brillouin zone illustrating **f**, peak intensity and **g,h**, fitted beam waists  $w_x$  ( $w_y$ ) in the  $x$ - ( $y$ -) directions. The system exhibits high uniformity, with relative standard deviations ( $\sigma$ ) of 2.6% for peak intensity and 3.1% (1.9%) for the  $w_x$  ( $w_y$ ).

### SINGLE-RIPA INTERFEROMETER CHARACTERIZATION

We first characterize the performance of a single RIPA by examining the interference pattern of its 1D phased array output, as shown in Fig. 2a. The array of beams exiting this RIPA (before the lens in Fig. 2a) are parallel and possess identical beam-shape; consequently, they focus to the same location in the image plane, with a common Gaussian envelope. Because the focusing beams after the lens intersect the image plane with unique transverse phase gradients, their summation is equivalent to a Fourier transform (as expected for a lens) of the beam array exiting the RIPA. The Fourier transform of these discrete beams produces a periodic series of interference peaks following multibeam diffraction pattern modulated by the common envelope of a single beam from the RIPA (see Methods). The displacement  $y$  of these interference peaks depends linearly on the phase difference  $\varphi_y$  between adjacent beams.

As illustrated in Fig. 2b, the interference of the phased array ( $N_y = 9$ ) produces a central feature whose  $1/e^2$  intensity radius is reduced from the width of the Gaussian envelope  $w_{\text{env}} = \frac{\lambda f}{\pi w_0} = 460 \mu\text{m}$  to  $w'_0 = \frac{\lambda f}{p} \sqrt{\frac{6}{\pi^2(N_y^2-1)}} = 14 \mu\text{m}$  (see Methods). The diffraction peaks (in higher Brillouin zones) are separated by  $L = \frac{\lambda f}{p} = 156 \mu\text{m}$ , consistent with the MLA pitch  $p$ . Depending on the ap-

plication, the ratio between the pitch  $p$  and the RIPA beam waist  $w_0$  can be tuned (e.g., using a MLA telescope, see Methods) to either distribute the power across multiple diffraction orders ( $p \gg w_0$ ) or concentrate most of the power within the first Brillouin zone ( $p \gtrsim w_0$ ).

In Fig. 2c, we probe the frequency response of the RIPA. The interference peak position  $y$  shifts linearly with optical frequency  $\nu$ , governed by  $y = \frac{\Delta\nu}{\text{FSR}_1} L$ . The frequency shift  $\Delta\nu$  is defined relative to the frequency where the accumulated phase  $\varphi_y$  satisfies  $\varphi_y \equiv 0 \pmod{2\pi}$ . The  $\text{FSR}_1 = \frac{c}{L_{\text{rt},1}} = 3.19 \text{ GHz}$  is the free spectral range (FSR) of the first RIPA, and equivalently, the total spectral bandwidth of the light exiting the RIPA spatial light modulator.

### CASCADED-RIPA MODULATOR CHARACTERIZATION

To form a 2D pattern, we direct the 1D phased array output of the first RIPA into the second RIPA, as shown in Fig. 1a. The cascaded system generates a 2D  $N_x \times N_y$  phased array with a phase profile of  $\varphi_{i,j} = i\varphi_x + j\varphi_y$ . As in the 1D case, all beams within the array share a common spatial mode profile, and their locations remain invariant under changes in laser frequency. Upon focusing, the 2D phased array generates a diffraction-limited spot whose position within the first Brillouin zone is con-

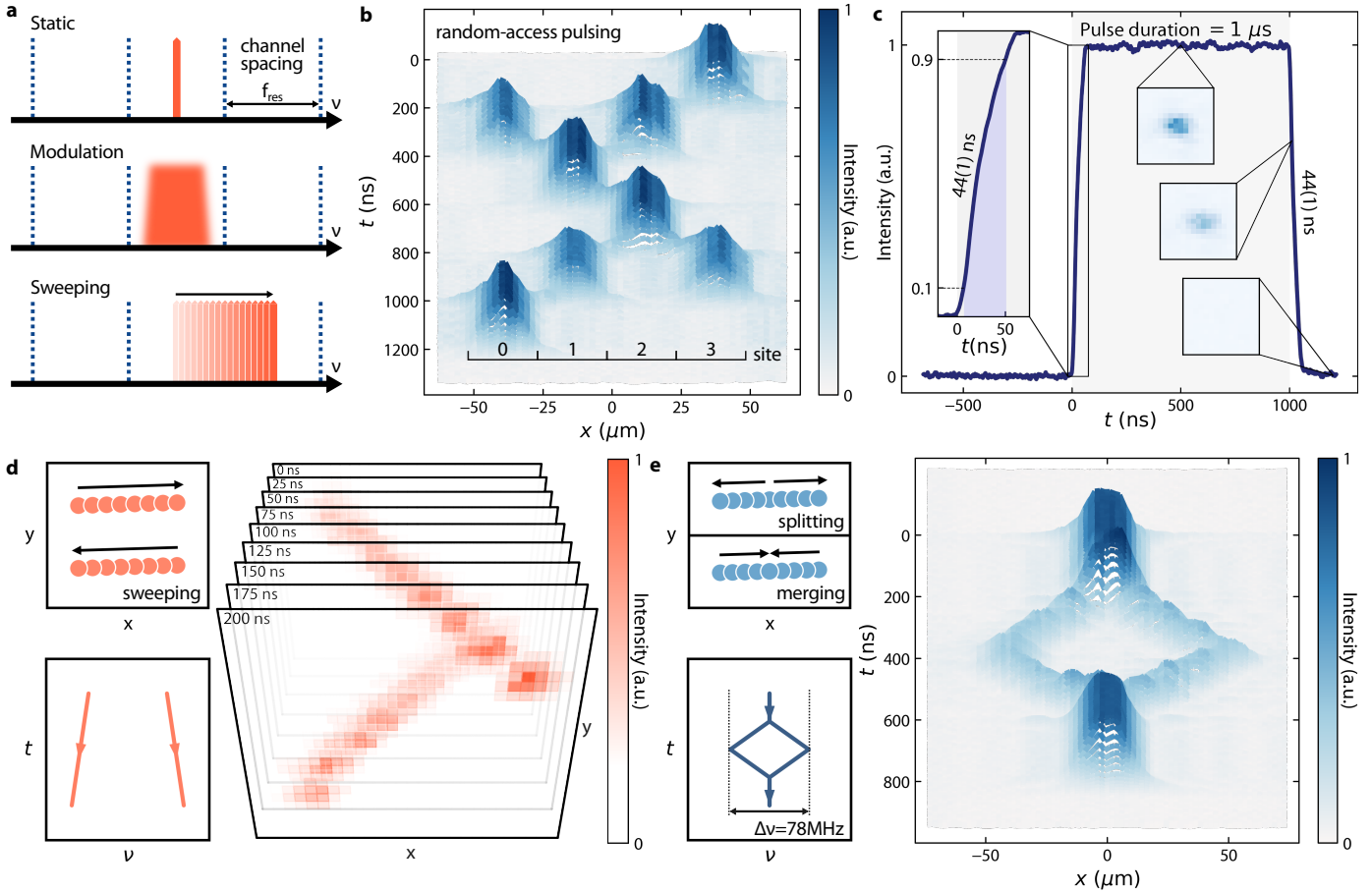


**FIG. 4. Dynamic operation of the RIPA spatial light modulator and time-resolved characterization.** **a**, Operational regimes of the RIPA SLM: *static* site addressing with channel spacing  $f_{\text{res}}$ ; *modulation* in amplitude (phase) which broadens the spectrum up to the channel spacing; and *sweeping* frequency to move the addressing site continuously in space. **b**, Fast random-access addressing across a four-site registry demonstrating independent amplitude modulation of individual SLM pixels. The plot displays vertically stacked line-cuts sampled every 4 ns using a scanning photodetector (PD). **c**, Temporal response of a 1  $\mu\text{s}$  optical pulse demonstrating symmetric 44(1) ns rise and fall times (10%–90%). The left inset zooms in on the rising edge. The three central insets depict 2D intensity distributions reconstructed from PD scans in the fully “on” state (top), during the transient (middle), and in the “off” state (bottom). **d**, Independent high-speed control of two spatially separated spots demonstrating continuous motion. Each spot corresponds to a distinct RF tone; independent motion of the respective spots in the image plane (insets). The main panel shows the spatiotemporal dynamics of two spots sweeping across the image plane at discrete time slices spanning  $\Delta t = 200$  ns. **e**, Programmable splitting and merging of a single spot. Starting from a single addressed spot, the RF drive is shaped to split the spot into two, translate each, and then recombine, as encoded by the frequency trajectories in the inset.

trolled by  $(\varphi_x, \varphi_y)$ , which is dependent on laser frequency  $\nu$ . We leverage this mapping to synthesize arbitrary spatial patterns with the cascaded-RIPA.

When the single-frequency phased array from the cascaded-RIPA is focused and imaged, the measured interference pattern exhibits a single, diffraction-limited spot (Fig. 3b), in analogy to the 1D case. Sweeping the laser frequency  $\nu$  rasters this spot across the Brillouin zone row-by-row (depicted schematically in Fig. 3a). A properly chosen set of optical tones produces the “S”-shaped pattern observed in Fig. 3c. It is composed of 11 individual spots, each corresponding to a distinct optical frequency  $\nu_k$ . These frequency components are synthe-

sized by phase-modulating a stabilized carrier ( $\nu^{\text{carrier}}$ ) using a broadband EOM which is itself driven by an arbitrary waveform generator (AWG). The AWG generates a multi-tone RF field  $E(t) = \sum_k A_k \cos(2\pi\nu_k^{\text{mod}}t + \phi_k)$ , consisting of a sum of frequency tones  $\{\nu_k^{\text{mod}}\}$  with amplitudes  $\{A_k\}$  and phases  $\{\phi_k\}$ , thereby generating optical sidebands at  $\nu_k = \nu^{\text{carrier}} + n \cdot \nu_k^{\text{mod}}$  ( $n \in \mathbb{Z}$ ) (Fig. 3d). We then employ a flat-top, sharp roll-off 2<sup>nd</sup>-order optical filter [41] ( $\sim 4$  GHz bandwidth) to suppress the optical carrier and unwanted modulation orders, selecting only the  $n = +1$  order for injection into the RIPA.

In Fig. 3e, we characterize system crosstalk by measuring the weighted optical power located at a distance

$d$  from a generated spot. Under the choice of different imaging systems, the distance  $d$  simultaneously scale with the spot waist  $w'_0$  ( $1/e^2$  intensity radius), thus the crosstalk naturally depends on the normalized distance  $d/w'_0$ . Due to the multi-beam interference nature of the spots, they exhibit power-law tails measured to be  $c(d) \sim \left(\frac{d}{w'_0}\right)^{-3.1}$  at large distances, rather than the exponential decay  $c(d) \sim \exp\left(-\frac{d^2}{w'^2_0}\right)$  of a Gaussian beam. The azimuthal average of this crosstalk reaches as low as  $2.8 \times 10^{-3}$  at a separation of  $d/w'_0 = 6.1$ . These results agree well with our theoretical model, with which we project a crosstalk of  $10^{-3}$  at a separation of 6.5 waists ( $d/w'_0 = 6.5$ ) and  $10^{-4}$  at a separation of 13.5 waists for a future  $100 \times 100$  RIPA modulator (see Methods).

The system also exhibits high uniformity, with the interference spot shape remaining largely invariant across the tuning range. This is expected given that the operating frequency range  $\text{FSR}_1 \approx 3 \text{ GHz}$  is negligible compared to the material dispersion, and the fact that the phased array maintains a fixed optical path independent of the laser frequency  $\nu$ . Uniformity maps (Fig. 3f-h) confirm a peak intensity standard deviation of 2.6% that could be further suppressed by finer control of RF signal amplitudes, while beam waist variations (3.1% in  $x$ , 1.9% in  $y$ ) remain below the camera pixel size.

## DYNAMIC OPERATION AND CHARACTERIZATION OF THE RIPA SLM

As illustrated in Fig. 4a, we can move beyond the *static* operation of the RIPA SLM by encoding arbitrary amplitude- or phase- modulation onto the existing frequency tones, which the RIPA spectrometer directly maps onto amplitude- or phase- modulation of the corresponding spots. The RIPA SLM thus promises a modulation bandwidth fundamentally governed by the spectral resolution (frequency channel spacing) of the constituent spectrometer, specifically  $f_{\text{res}} = c/(N_x L_{\text{rt},2}) = 16 \text{ MHz}$ . Beyond discrete addressing, continuous frequency *sweeping* facilitates smooth motion of the corresponding spots along the fast-moving axis in the raster scan pattern. Such dynamic operations leverage frequency-bin encoding, which is intrinsically crosstalk-free (up to the Fourier limit) and supports parallel, independent control.

In Fig. 4, we characterize the temporal response of the RIPA SLM and demonstrate its continuous operation with dynamical reconfiguration. Since the RIPA SLM operates faster than any commercially available camera [42], we employ a high-speed photodetector (PD) on a 2D translation stage as our “camera” (see Methods) to resolve the optical dynamics. This approach achieves a 2 ns temporal resolution and a  $5 \mu\text{m}$  spatial resolution. We first demonstrate random-access addressing across a four-site registry arranged in a line, as shown in Fig. 4b. The plot shows stacked line-cuts through the registry with 4 ns spacing, demonstrating fast and independent local

control with a 200 ns switching time and negligible cross-site interference.

We further examine the switching speed of the RIPA SLM by pulsing a single frequency component. As shown in Fig. 4c, we drive the EOM with a 1  $\mu\text{s}$  pulse and record the PD response integrated over a  $(75 \mu\text{m})^2$  region (central insets) and observe a smooth and rapid transition at the pulse edge. The 10%-90% rise- and fall- times are measured to be 44(1) ns, showing shot-to-shot stability across all spatial locations. During the “on” state, the intensity settles to within 0.68% of its peak value. The measured 44 ns rise-time and the associated temporal dynamics are in quantitative agreement with our theoretical model, which is dominated by the 7.7 ns round-trip propagation time in the second RIPA and the 50 MHz photodetector bandwidth (see Methods). Furthermore, the beam maintains a well-defined spatial profile during both the “on” state and the transient period (central insets of Fig. 4c).

Finally, we showcase complex spatio-temporal modulation by independently moving two spots across the field of view. As shown in Fig. 4d, linear RF frequency ramps drive continuous motion of two spots across the image plane over 200 ns, without shape distortion or mutual interference. This confirms its capability of parallel, continuous movement of beams with arbitrary non-outer-product patterns. The lensing effect [34] arising from frequency chirping is calculated and numerically confirmed to be two orders of magnitude smaller than in AODs (see Methods). In Fig. 4e, we split a single spot into two spots and then recombine them to examine a scenario where spots intersect. Stacked line-cuts along the beam splitting direction with 4 ns spacing reveals no substantial interference, which is attributed to the low crosstalk of the RIPA SLM. Moreover, any residual intensity oscillations should occur at the beat frequency (here 78 MHz). For atomic physics applications, these oscillations are fast compared to sub-MHz atom motion and MHz gates, and are thus largely decoupled.

## OUTLOOK

We demonstrate a high-speed two-dimensional optical display capable of performing fully-independent site-resolved addressing at an effective frame rate exceeding 10 MHz. The device is powered by a first-of-its-kind ultra-high-resolution spectrometer based on a novel interferometer architecture — the Re-Imaging Phased Array, which achieves its spectral sensitivity through long path lengths and stabilizes its spatial mode through re-imaging lens-guides. The device implements high-bandwidth and low-crosstalk frequency-to-spatial optical decoding from single-wire electrical modulation in the frequency domain.

By minimizing round-trip power loss and adopting custom micro-fabricated optics (see Methods), scaling the current system to a  $100 \times 100$  arrays and beyond (which

does not require increasing the total footprint, see Methods) will unlock numerous application domains: Foremost among these is the realization of optical tweezer arrays with dynamically reconfigurable trapping potentials for neutral atom quantum computing, where the RIPA SLM provides scalable, parallel, and independent atom motion to facilitate efficient quantum error correction (QEC) schemes [24, 32, 43, 44] and continuous atom replacement [20–22]. Furthermore, integration with recent three-dimensional control techniques [45–47] will enable high-speed, collision-free atom rearrangement. Beyond quantum information science, the RIPA has myriad applications ranging from ultra-precision spectroscopy [38, 48, 49] and narrow-band frequency multiplexing for quantum networks [50–53] to MHz-rate random-access volumetric microscopy [28, 29], all-optical neural interrogation for optogenetics [28], as well as agile beam steering for next-generation free-space communication and LiDAR [54, 55].

### Acknowledgments

We thank Bowen Li for helpful discussions and feedback during the drafting of this paper. We thank Marius Jürgensen for his valuable input on the geometric de-

sign. This work was supported by the Office of Naval Research (ONR) through Grant N000142512291, and by the National Science Foundation (NSF) through QLCI-HQAN grant 2016136. Z.L. acknowledges support from the Urbanek-Chodorow Fellowship. A.L.S. is supported by the Stanford Science Fellowship, and additionally by the Felix Bloch Fellowship and the Urbanek-Chodorow Fellowship.

### AUTHOR CONTRIBUTIONS

X.W., Z.L., and A.V.K. performed the experiments. X.W., Z.L., A.L.S., A.V.K. contributed to data analysis. X.W., Z.L., J.S., and D.I.S. contributed to prototypes of the experimental geometry. X.W., Z.L. and J.S. wrote the manuscript with contributions and input from all authors. D.I.S. and J.S. supervised this project. X.W. and Z.L. contributed equally.

### COMPETING INTERESTS

J.S. acts as a consultant to and holds stock options from Atom Computing. X.W., Z.L., A.V.K., D.I.S. and J.S. hold a patent on the phased array geometry described in this work.

---

[1] Hell, S. W. Far-field optical nanoscopy. *Science* **316**, 1153–1158 (2007).

[2] Vettenburg, T. *et al.* Light-sheet microscopy using an airy beam. *Nature Methods* **11**, 541–544 (2014).

[3] Fahrbach, F. O., Simon, P. & Rohrbach, A. Microscopy with self-reconstructing beams. *Nature photonics* **4**, 780–785 (2010).

[4] Takeda, M., Ina, H. & Kobayashi, S. Fourier-transform method of fringe-pattern analysis for computer-based topography and interferometry. *Journal of the optical society of America* **72**, 156–160 (1982).

[5] Richardson, D. J., Fini, J. M. & Nelson, L. E. Space-division multiplexing in optical fibres. *Nature photonics* **7**, 354–362 (2013).

[6] Bozinovic, N. *et al.* Terabit-scale orbital angular momentum mode division multiplexing in fibers. *science* **340**, 1545–1548 (2013).

[7] Steinhauer, J. Observation of quantum hawking radiation and its entanglement in an analogue black hole. *Nature Physics* **12**, 959–965 (2016).

[8] Clark, L. W., Gaj, A., Feng, L. & Chin, C. Collective emission of matter-wave jets from driven bose-einstein condensates. *Nature* **551**, 356–359 (2017).

[9] Chiu, C. S., Ji, G., Mazurenko, A., Greif, D. & Greiner, M. Quantum state engineering of a hubbard system with ultracold fermions. *Phys. Rev. Lett.* **120**, 243201 (2018).

[10] Yan, Z. *et al.* Superradiant and subradiant cavity scattering by atom arrays. *Phys. Rev. Lett.* **131**, 253603 (2023).

[11] Yamazaki, R., Taie, S., Sugawa, S. & Takahashi, Y. Sub-micron spatial modulation of an interatomic interaction in a bose-einstein condensate. *Phys. Rev. Lett.* **105**, 050405 (2010).

[12] Baum, C., Jaffe, M., Palm, L., Kumar, A. & Simon, J. Optical mode conversion via spatiotemporally modulated atomic susceptibility. *Optics Express* **31**, 528–535 (2022).

[13] Orsi, F. *et al.* Cavity microscope for micrometer-scale control of atom-photon interactions. *PRX Quantum* **5**, 040333 (2024).

[14] Marsh, B. P. *et al.* Multimode cavity qed ising spin glass. *Phys. Rev. Lett.* **135**, 160403 (2025).

[15] Graham, T. *et al.* Multi-qubit entanglement and algorithms on a neutral-atom quantum computer. *Nature* **604**, 457–462 (2022).

[16] Radnaev, A. *et al.* Universal neutral-atom quantum computer with individual optical addressing and nondestructive readout. *PRX Quantum* **6**, 030334 (2025).

[17] Manetsch, H. J. *et al.* A tweezer array with 6100 highly coherent atomic qubits. *Nature* **647**, 60–67 (2025).

[18] Endres, M. *et al.* Atom-by-atom assembly of defect-free one-dimensional cold atom arrays. *Science* **354**, 1024–1027 (2016).

[19] Lam, M. R. *et al.* Demonstration of quantum brachistochrones between distant states of an atom. *Phys. Rev. X* **11**, 011035 (2021).

[20] Chiu, N.-C. *et al.* Continuous operation of a coherent 3,000-qubit system. *Nature* **646**, 1075–1080 (2025).

[21] Li, Y., Bao, Y., Peper, M., Li, C. & Thompson, J. D. Fast, continuous and coherent atom replacement in a neutral atom qubit array (2025). 2506.15633.

[22] Chow, M. N. H. *et al.* Circuit-based leakage-to-erasure conversion in a neutral-atom quantum processor. *PRX Quantum* **5**, 040343 (2024).

[23] Bluvstein, D. *et al.* Logical quantum processor based on reconfigurable atom arrays. *Nature* **626**, 58–65 (2024).

[24] Guo, J., Hong, Y., Kaufman, A. & Lucas, A. Toward self-correcting quantum codes for neutral atom arrays. *PRX Quantum* **7**, 010301 (2026).

[25] Brown, M., Thiele, T., Kiehl, C., Hsu, T.-W. & Regal, C. Gray-molasses optical-tweezer loading: controlling collisions for scaling atom-array assembly. *Physical Review X* **9**, 011057 (2019).

[26] Bluvstein, D. *et al.* A quantum processor based on coherent transport of entangled atom arrays. *Nature* **604**, 451–456 (2022).

[27] Zhao, M. *et al.* An integrated photonics platform for high-speed, ultrahigh-extinction, many-channel quantum control. *arXiv preprint arXiv:2508.09920* (2025).

[28] Katona, G. *et al.* Fast two-photon in vivo imaging with three-dimensional random-access scanning in large tissue volumes. *Nature methods* **9**, 201–208 (2012).

[29] Yamaguchi, A. *et al.* Multi-neuronal recording in unrestrained animals with all acousto-optic random-access line-scanning two-photon microscopy. *Frontiers in Neuroscience* **17**, 1135457 (2023).

[30] Eastin, B. & Knill, E. Restrictions on transversal encoded quantum gate sets. *Phys. Rev. Lett.* **102**, 110502 (2009).

[31] Pogorelov, I. *et al.* Experimental fault-tolerant code switching. *Nature Physics* **21**, 298–303 (2025).

[32] Bravyi, S. *et al.* High-threshold and low-overhead fault-tolerant quantum memory. *Nature* **627**, 778–782 (2024).

[33] Zhang, B., Peng, P., Paul, A. & Thompson, J. D. Scaled local gate controller for optically addressed qubits. *Optica* **11**, 227–233 (2024).

[34] Dickson, L. D. Optical considerations for an acoustooptic deflector. *Applied Optics* **11**, 2196–2202 (1972).

[35] Zhang, B. *et al.* Leveraging erasure errors in logical qubits with metastable  $^{171}\text{yb}$  atoms (2025). 2506.13724.

[36] Shirasaki, M. Large angular dispersion by a virtually imaged phased array and its application to a wavelength demultiplexer. *Optics Letters* **21**, 366–368 (1996).

[37] Chan, T., Myslivets, E. & Ford, J. E. 2-dimensional beamsteering using dispersive deflectors and wavelength tuning. *Optics Express* **16**, 14617–14628 (2008).

[38] Sadiek, I., Lang, N. & Van Helden, J.-P. H. Air-spaced virtually imaged phased array with 94 mhz resolution for precision spectroscopy. *Optics Express* **32**, 46511–46521 (2024).

[39] Jaffe, M. *et al.* Understanding and suppressing backscatter in optical resonators. *Optica* **9**, 878–885 (2022).

[40] Shadmany, D. *et al.* Cavity qed in a high na resonator. *Science Advances* **11**, eads8171 (2025).

[41] Li, Z., Karve, A. V., Wei, X. & Simon, J. A second-order optical butterworth fabry-pérot filter (2025). 2510.15032.

[42] Li, B. *et al.* Mega-fps low light camera. *Optics Express* **33**, 31096–31106 (2025).

[43] Hong, Y., Marinelli, M., Kaufman, A. M. & Lucas, A. Long-range-enhanced surface codes. *Phys. Rev. A* **110**, 022607 (2024).

[44] Sahay, K., Jin, J., Claes, J., Thompson, J. D. & Puri, S. High-threshold codes for neutral-atom qubits with biased erasure errors. *Phys. Rev. X* **13**, 041013 (2023).

[45] Lu, Y.-H. *et al.* Astigmatism-free 3d optical tweezer control for rapid atom rearrangement (2025). 2510.11451.

[46] Guo, Z., van Herk, R. A. H., Vredenbregt, E. J. D. & Kokkelmans, S. J. J. M. F. Acousto-optic lens for 3d shuttling of atoms in a neutral atom quantum computer (2025). 2510.09398.

[47] Picard, L. R. B. & Endres, M. A three-dimensional acousto-optic deflector (2025). 2510.07633.

[48] Nugent-Glandorf, L. *et al.* Mid-infrared virtually imaged phased array spectrometer for rapid and broadband trace gas detection. *Optics letters* **37**, 3285–3287 (2012).

[49] Liang, Q., Bisht, A., Scheck, A., Schunemann, P. G. & Ye, J. Modulated ringdown comb interferometry for sensing of highly complex gases. *Nature* **638**, 941–948 (2025).

[50] Wengerowsky, S., Joshi, S. K., Steinlechner, F., Hübel, H. & Ursin, R. An entanglement-based wavelength-multiplexed quantum communication network. *Nature* **564**, 225–228 (2018).

[51] Komza, L. *et al.* Multiplexed color centers in a silicon photonic cavity array. *Optica* **12**, 1400–1405 (2025).

[52] Sinclair, N. *et al.* Spectral multiplexing for scalable quantum photonics using an atomic frequency comb quantum memory and feed-forward control. *Phys. Rev. Lett.* **113**, 053603 (2014).

[53] Pu, Y. *et al.* Experimental realization of a multiplexed quantum memory with 225 individually accessible memory cells. *Nature communications* **8**, 15359 (2017).

[54] Lin, S., Chen, Y. & Wong, Z. J. High-performance optical beam steering with nanophotonics. *Nanophotonics* **11**, 2617–2638 (2022).

[55] Hail, C. U., Michaeli, L. & Atwater, H. A. Ultrafast, reconfigurable all-optical beam steering and spatial light modulation (2025). 2511.03860.

[56] Wei, X. optable. URL <https://github.com/tim4431/optable>.

[57] Wei, X. vipa focus simulation. URL [https://github.com/tim4431/vipa\\_focus\\_simulation](https://github.com/tim4431/vipa_focus_simulation).

[58] Zupancic, P. *et al.* Ultra-precise holographic beam shaping for microscopic quantum control. *Optics express* **24**, 13881–13893 (2016).

[59] Bradski, G. The OpenCV Library. *Dr. Dobb's Journal of Software Tools* (2000).

[60] Sommer, A. & Simon, J. Engineering photonic floquet hamiltonians through fabry-pérot resonators. *New Journal of Physics* **18**, 035008 (2016).

## Data Availability

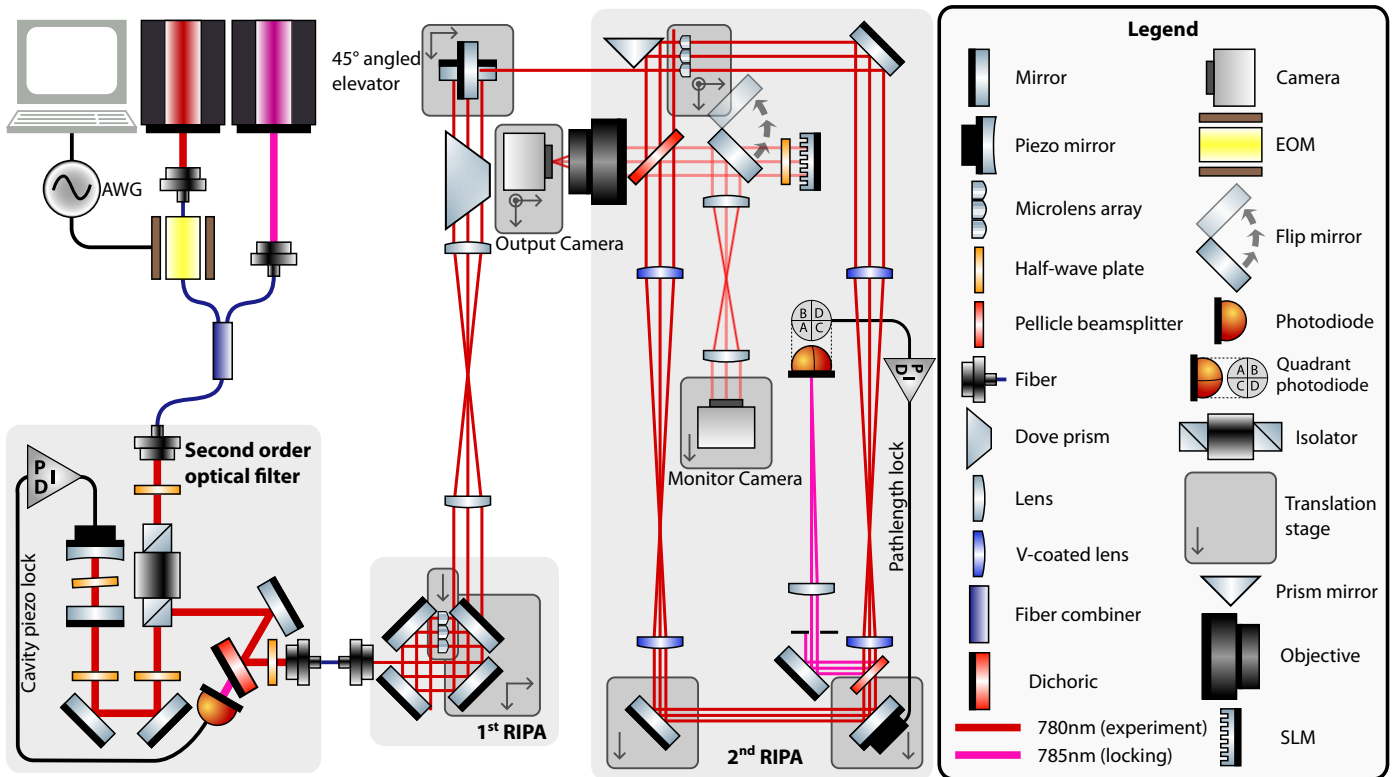
The experimental data presented in this manuscript are available from the corresponding author upon request, due to the proprietary file formats employed in the data collection process.

## Code Availability

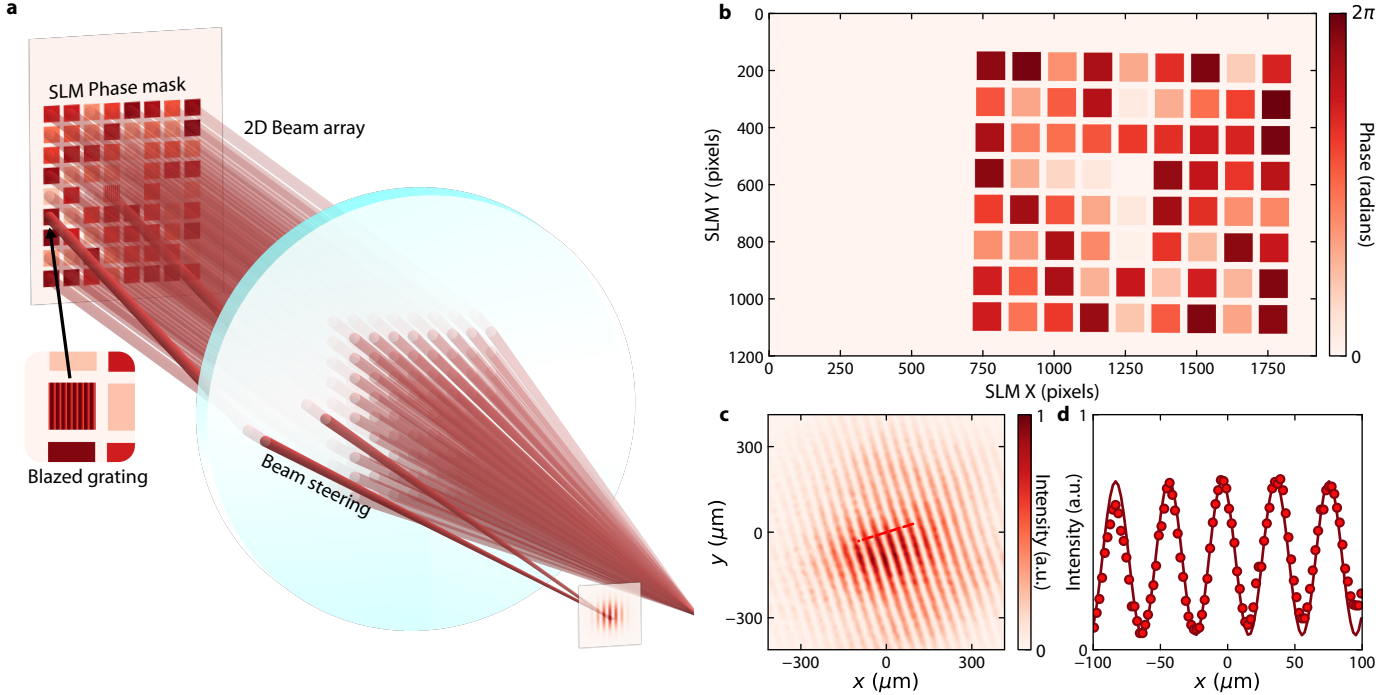
The source code for simulations and performing experiments are available from the corresponding author

upon request. Codes for RIPA ray-tracing are available at Ref. [56]. Codes for simulating the interference pattern are available at Ref. [57].

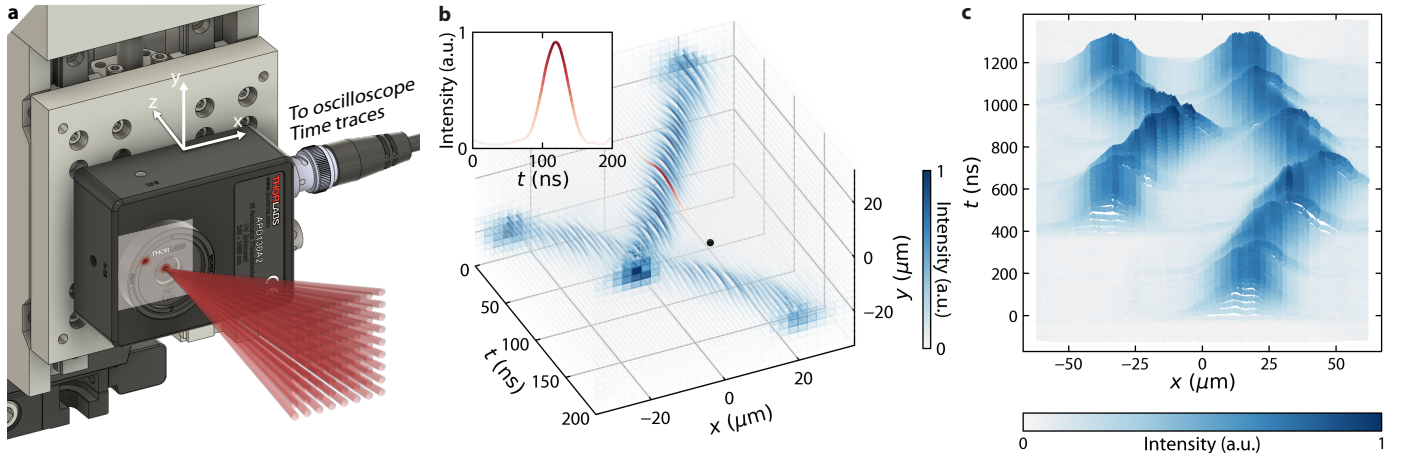
## EXTENDED DATA FIGURES



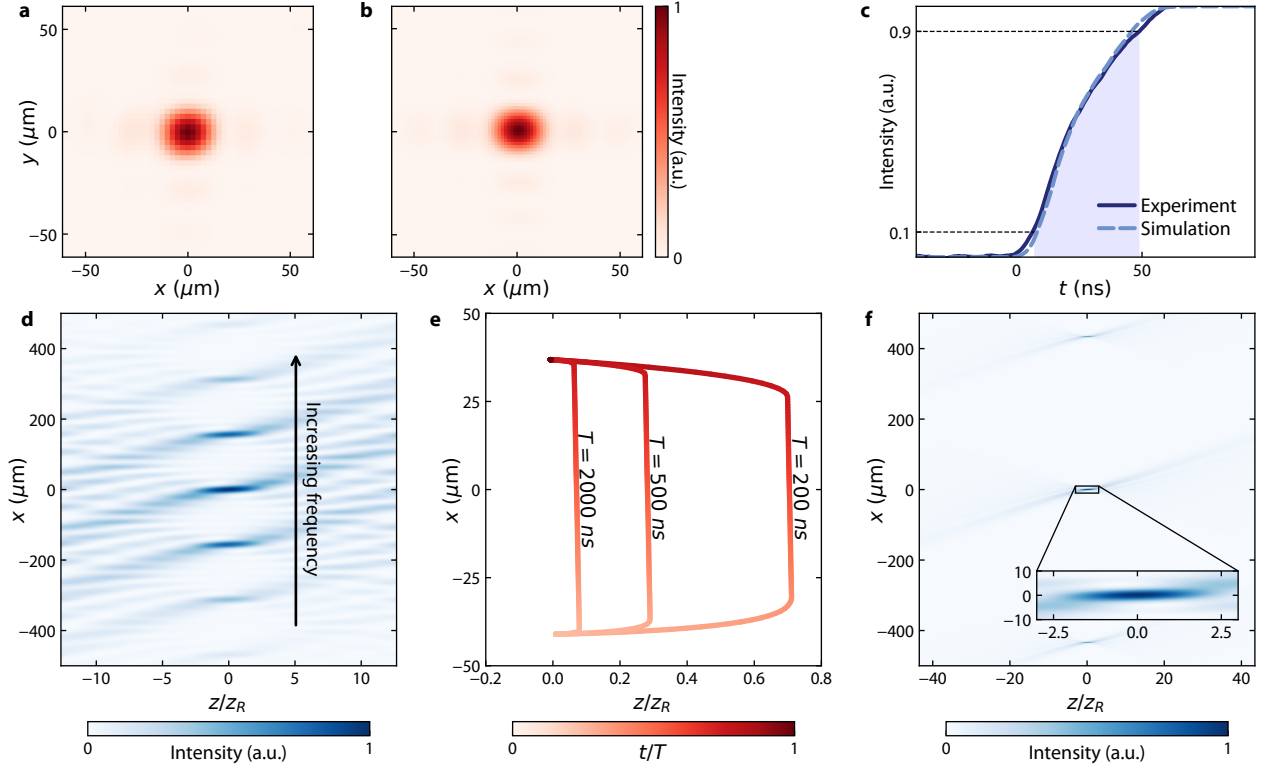
Ext. Data Fig. 1. **Detailed schematic of the RIPA system.** The experiment operates with a 780 nm source (red paths), while an auxiliary 785 nm laser (pink paths) provides active path-length stabilization. Input frequency tones are generated by phase-modulation using an electro-optic modulator (EOM) driven by an arbitrary waveform generator (AWG). A second-order optical filter isolates the +1 modulation sidebands and injects them into the first RIPA. The first RIPA converts the input into a 1D beam array using a microlens array (MLA). This array is transferred via a 4f relay which contains angled elevator mirrors and a Dove prism for spatial alignment (tilt, displacement, and roll) to the second RIPA. The second RIPA employs the same MLA and V-coated 4f telescopes to generate a 2D beam array. A pellicle beamsplitter out-couples the light to a spatial light modulator (SLM) for phase calibration (see Ext. Data Fig. 2) and final imaging (with static phase mask). Active locking of the second RIPA path length is achieved via quadrant photodiodes and piezo-actuated mirrors. Pairs of mirrors mounted on translation stages allow for the independent tuning of round-trip path length and beam separation to match the MLA pitch.



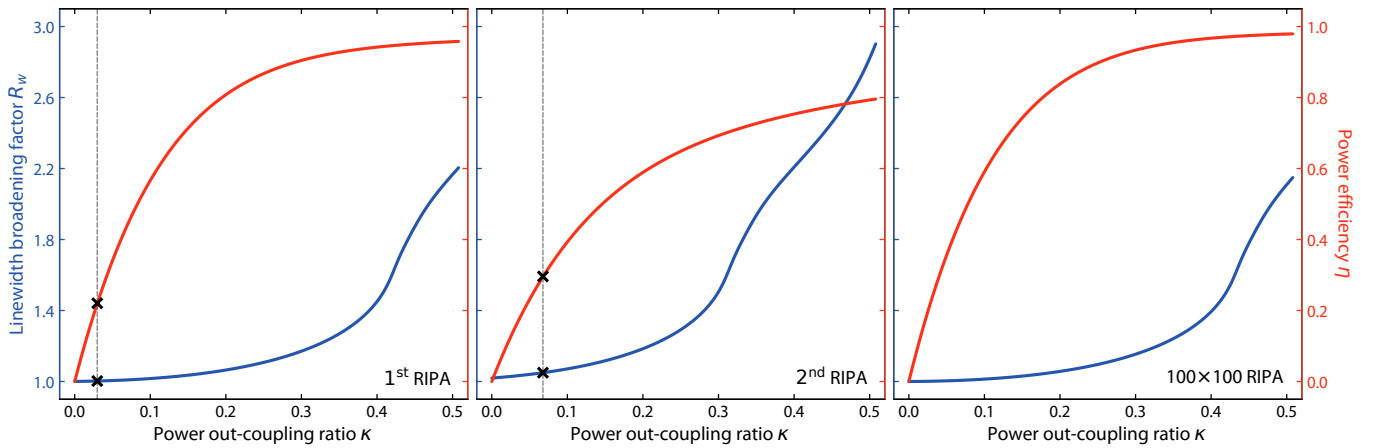
Ext. Data Fig. 2. **Interferometric calibration of SLM phase mask.** **a**, Schematic of the phase calibration procedure. Localized blazed gratings are applied to specific sub-regions of the SLM to steer pairs of beams from the 2D beam array, causing them to interfere at the focal plane. This process compensates for *static* wavefront aberrations and ensures phase uniformity across the array. **b**, The resulting calibrated phase mask. Each grid tile consists of  $100 \times 100$  SLM pixels (covering an  $800 \times 800 \mu\text{m}^2$  area), providing independent phase control for each beam in the array. **c**, Representative interference fringes captured at the focal plane. **d**, One-dimensional intensity line-cut (dots) of the fringes in **c** with a sinusoidal fit (solid line), from which the relative phase is extracted for precise compensation.



Ext. Data Fig. 3. **Scanning photodetector for resolving nano-second beam dynamics.** **a**, A photodetector (PD) with a  $5 \mu\text{m}$  diameter pinhole is mounted on a 3-axis translation stage to sample the focal plane. Synchronized triggering of the AWG which drives the EOM and an oscilloscope records the PD voltage with 2 ns temporal resolution. **b**, Spatio-temporal reconstruction. Raw time-traces recorded at discrete spatial coordinates (inset) are synthesized into a spatio-temporal intensity distribution (data corresponds to Fig. 4d). Stacking these time traces yields a movie of spot dynamics with  $5 \mu\text{m} \times 5 \mu\text{m}$  spatial and 2 ns temporal resolution. **c**, Reconstructed 1D trajectories of spots showing the asynchronous motion of two independent spots following a zigzag trajectory.



Ext. Data Fig. 4. **Simulated interference patterns and experimental validation.** **a,b**, Comparison of experimental **a** and simulated **b** focal-plane intensity distributions ( $xy$  cross-section). **c**, Temporal evolution of the integrated intensity for the pulse sequence described in Fig. 4c. The experimental data (solid dark blue) agrees with the simulation (dashed light blue). **d**, Simulated beam profile in the  $xz$  plane. The axial coordinate  $z$  is normalized by the Rayleigh range  $z_R$ . The interference pattern exhibits a localized Gaussian beam profile near the focal point. **e**, Transient axial focal shift during linear frequency chirping. The traces show the trajectory of the beam waist in the  $xz$  plane for various sweep durations ( $T = 200, 500$ , and  $2000$  ns) for the same transverse displacement, illustrating the dynamic lensing effect. **f**, Simulated  $xz$  cross-section of the scaled-up  $100 \times 100$  RIPA configuration. The inset provides a magnified view of the beam waist, demonstrating tight confinement.



Ext. Data Fig. 5. **Tradeoff between power efficiency and interference linewidth.** Calculated power efficiency  $\eta$  (red, right axis) and the interference linewidth broadening factor  $R_w$  (blue, left axis) as functions of the power out-coupling ratio  $\kappa$  for the first RIPA (left), the second RIPA (center), and the proposed  $100 \times 100$  RIPA (right) configurations. In each panel, vertical dashed lines and the black crosses denote the experimental operating points.

## METHODS

### 1. Description of the experiment

Here we describe the architecture of the experimental system, focusing on frequency tone generation, the geometry of the RIPA system, and wavefront correction via a SLM. A comprehensive schematic of the layout is provided in Ext. Data Fig. 1.

#### Frequency tone generation

Optical frequency tones corresponding to the target spatial profile are synthesized by phase-modulating a 780 nm laser using an EOM (Thorlabs LNY7810A) driven by a high-speed AWG (Keysight M8195A, 65GSa/s). The AWG is programmed to generate a multi-tone RF waveform  $V(t) = \frac{1}{\sum_{k=1}^N A_k} \sum_{k=1}^N A_k \cos(2\pi\nu_k^{\text{mod}} t + \phi_k)$ , where  $\nu_k^{\text{mod}}$  denotes the RF modulation frequency (centered at 11 GHz), while  $A_k$  and  $\phi_k$  represent the amplitude and phase of each constituent frequency tone, respectively.

This RF signal is boosted via a two-stage amplifier chain (Minicircuits ZX60-10223G+ and RF Bay MGA-22-13) to attain powers of  $\approx +16\text{dBm}$  for a single tone and  $\approx -7\text{dBm}$  per tone for  $\sim 100$  tones. To isolate the target spectrum, we build a second-order Butterworth-type optical filter [41] and actively lock it to the +1 sideband. The filter optically selects only the +1 modulation sidebands with a flat-band response over a  $\sim 4$  GHz bandwidth and has a high rejection for the carrier and other unwanted sidebands.

#### The geometry of RIPA

As shown in Ext. Data Fig. 1, the experiment operates at 780 nm (red paths), while an auxiliary 785 nm laser (pink) is used for path-length stabilization. The first RIPA converts the input beam into a 1D beam array using a MLA that re-images the beams during each round trip. A 4f relay transfers this 1D beam array to the input of the second RIPA, where a pair of 45° angled elevator mirrors controls the beam tilt and displacement, and a dove prism adjusts the roll angle. The second RIPA employs an identical MLA inside its round trip, supplemented by two 4f path-length extension telescopes whose lenses are V-coated for 780 nm (reflection  $< 0.1\%$ ) to minimize loss. A pellicle beamsplitter (Thorlabs BP108) inside the second RIPA round trip acts as an outcoupler, directing the resulting 2D beam array at normal incidence onto a SLM for static phase compensation, as described in a later section. The corrected phased array is then focused onto the output camera; alternatively, a flip mirror can redirect it to a monitor camera on an

equivalent Fourier plane, where the beams are of equal size and propagate in parallel.

The 785 nm auxiliary laser (pink paths) simultaneously stabilizes optical filter cavity and the second RIPA path length. For the latter, two adjacent beams from the 2D beam array are spatially isolated and interfered at a quadrant photodiode (Thorlabs PDQ80A). The resulting error signal is fed to a piezo actuator to lock the round-trip path length of second RIPA.

System alignment is performed by iteratively matching the beam separation to the MLA pitch ( $p$ ) and matching the effective round-trip path length to the target round-trip length which supports the fundamental lens-guide mode. To decouple these two degrees of freedom, we utilize either mirror pairs mounted on translation stages or individual mirrors on separate motorized stages controlled via common- and differential-mode actuation. Further details on the alignment protocol are available in Supplementary Information.

#### SLM phase correction

The interference pattern of the 2D beam array is highly sensitive to optical aberrations and surface roughness, which can significantly degrade its quality. Since the beam array is nicely discretized in space before the focusing lens, we can compensate for these phase errors immediately after the out-coupling pellicle beamsplitter using a SLM (Meadowlark E-Series, 1920x1200, 8-Bit) to apply a *static* phase mask. Once calibrated, this mask remains consistent throughout the operation of the RIPA SLM.

The calibration procedure is performed as follows. First, we map the 2D beam array indexed with  $(i, j)$  onto the SLM pixel coordinates  $(x, y)$ . To achieve this, we employ a 4f imaging system to image the  $N_x \times N_y$  array reflected from the SLM, with an iris in the Fourier plane for spatial filtering. Applying a blazed-grating pattern to the SLM deflects specific beams so they are blocked by the iris. By narrowing the grating region via binary search and sliding-window procedures, we precisely determine the coordinate  $(x, y)_{ij}$  for each beam  $(i, j)$ . By determining the  $(x, y)_{ij}$  for a set of selected beams (e.g.,  $(i, j) = (0, 0), (0, N_y - 1), (N_x - 1, 0)$ ), the coordinates for the entire array are obtained via an affine transformation fit.

Next, we calibrate the relative phase  $\phi_{ij}$  between the beam  $(i, j)$  and a reference beam  $(i_R, j_R)$  [58]. As shown in Ext. Data Fig. 2, the SLM isolates the reference beam  $(i_R, j_R)$  and the target beam  $(i, j)$  out by applying local blazed-grating masks. We extract the relative phase from their interference pattern in the Fourier plane (Ext. Data Fig. 2c). The line-cut intensity (Ext. Data Fig. 2d) is fitted to  $I(x) = I_0(1 + \gamma \cos(2\pi f x + \phi_{ij}))$ , where  $\phi_{ij}$  is the phase difference relative to the reference. The origin of the coordinate axis  $x$  is kept fixed for different  $(i, j)$  beams.

During the calibration, the laser frequency and the round-trip length of the second RIPA are actively stabilized to ensure fringe stability. After calibration, the calibrated phase mask (Ext. Data Fig. 2b) is applied to compensate for wavefront distortions. Given the  $\sim 3$ GHz spectral bandwidth, chromatic dispersion is negligible. Consequently, the calibration remains valid and maintains high interference quality across the entire operating frequency range.

## 2. Characterization of RIPA

Here we present the methods used to characterize the RIPA in terms of its frequency-domain response (Fig. 3, static, data acquired with a camera), and its time-domain dynamics (Fig. 4, transient, data acquired with a scanning photodetector).

### Frequency-domain (static) characterization

We detail the methods used to characterize the frequency-domain response of RIPA shown in Fig. 3.

First, we calibrate the RF frequency and amplitude responses of the system. We vary the RF modulation frequency  $\nu_k^{\text{mod}}$  from 9 to 13 GHz and measure the power in the  $+1$  sideband ( $I$ ) after the EOM and filter. The RF amplitude response is similarly calibrated by varying the RF output amplitude  $A_k$  across the 8-Bit AWG range (0-255); see Supplementary Information for the calibration curve.

Leveraging the calibration data  $I(\nu_k^{\text{mod}}, A_k)$ , we generate highly uniform arbitrary patterns and characterize their quality. We drive the EOM with a single RF frequency and sweep across the first RIPA's free spectral range ( $\text{FSR}_1 \sim 3$  GHz) over an  $11 \times 11$  grid to characterize the interference peaks within the first Brillouin zone. Given  $R = \text{FSR}_1/\text{FSR}_2 \approx 24.6$ , we modulate the frequencies as  $\nu_{k=(i,j)}^{\text{mod}} = (2 \cdot i + j/N) \cdot \text{FSR}_2$  to address a quasi-squared grid. The RIPA SLM routes these tones to the image plane in a near-orthogonal grid (with relative angle  $\theta = \pi/2 - \arctan(1/R)$ ). The resulting spacings of the “grid” are  $d_x = \frac{f\lambda}{p} \frac{1}{N} = 14.2 \mu\text{m} \sim w'_0$ , and  $d_y = \frac{f\lambda}{p} \frac{2}{R} = 12.7 \mu\text{m} \lesssim w'_0$ . A careful choice of  $R = \text{FSR}_1/\text{FSR}_2 = N = N_x = N_y$  and  $\nu_{k=(i,j)}^{\text{mod}} = (i + j/N) \cdot \frac{1}{1+1/R^2} \cdot \text{FSR}_2$  will generate an orthogonal square grid  $d_x = d_y \sim w'_0$ , achieving the optimal frequency-to-spatial mapping for 2D site-resolved addressing (see Supplementary Information).

We image the RIPA SLM focal plane using a Basler camera (a2A5060-15umBAS), which blocks the 785 nm locking-path light by a 780 nm MaxLine filter (Semrock, LL01-780). Using OpenCV [59], we extract interference peak positions and apply local 2D Gaussian fits to determine the  $1/e^2$  waists ( $w_x, w_y$ ) and peak intensities ( $I$ ). This fitting is valid because the interference pattern lo-

cally resembles a 2D Gaussian (details in later sections). Site-resolved heatmaps of (Fig. 3g-h) show standard deviations of  $\sigma = 3.1\%$  for  $w_x$  and  $\sigma = 1.9\%$  for  $w_y$ , respectively.

Despite RF system calibration, the intensities  $I$  are modulated by a Gaussian envelope which is the Fourier transform of the individual beams' common spatial mode. By extracting and compensating for this envelope using the camera data, we achieve an intensity homogeneity of  $\sigma = 2.6\%$  (Fig. 3f).

To assess the system's suitability for optical site-addressing, we calibrate the crosstalk (Fig. 3e), defined as the Gaussian-weighted optical power encircled within a waist  $w'_0$  at a site located a distance  $d$  from an addressed site. The experimental results for an  $(N_x, N_y) = (8, 9)$  array align well with the theoretical model, accounting for measured power attenuation of 19.8% (5.2%) per  $x(y)$  round trip; these values include out-coupling ratios of 6.8% (3.0%) per round trip. This suggests that for a  $(N_x, N_y) = (100, 100)$  array with a 1% loss per round trip in both RIPAs (red curve, Fig. 3e), crosstalk would reach  $10^{-3}$  at a separation of 6.5 waists and  $10^{-4}$  at a separation of 13.5 waists.

The multi-beam interference nature causes the second-largest interference peak to maintain an intensity of  $(\frac{2}{3\pi})^2 \approx 4.5\%$  relative to the main peak, regardless of the number of beams  $N$ . See Supplementary Information for the figures. These significant interference “tails” drive the power-law scaling of crosstalk observed in Fig. 3e. Conversely, this enables operation in a closely-packed regime where  $d_{x,y} = \frac{f\lambda}{p} \frac{1}{N_{x,y}}$ ; at this grid spacing, each spot coincides with a null in the field of its neighbors. We also report crosstalk scaling curves along the x- axis and the diagonal axis, see Supplementary Information.

### Time-domain (transient) characterization

We detail the methods used to characterize the nanosecond-scale time-domain dynamics of RIPA SLM using a scanning photodetector, as presented in Fig. 4.

The measurement principle of the scanning photodetector method relies on capturing repeatable time-resolved response of the RIPA focal plane at discrete spatial coordinates. By physically translating the photodetector across the target region, we reconstruct the full spatiotemporal evolution of the optical field.

As shown in Ext. Data Fig. 3a, we place a  $5 \mu\text{m}$ -diameter pinhole (Thorlabs P5K) in front of an avalanche photodiode (APD, Thorlabs APD130A2), which is mounted on a three-axis translation stage. The detector is precisely positioned along the  $z$ -axis to coincide with the focal plane ( $xOy$ ). At each scanning coordinate, the control PC initiates a trigger to synchronize the AWG and an oscilloscope. Once triggered, the AWG then generates the programmed RF pulse sequences to drive the EOM, while the oscilloscope records the APD voltage traces (Ext. Data Fig. 3b, inset) with 2 ns tem-

poral resolution. By systematically acquiring time traces over a 2D grid covering the first Brillouin zone with  $5\ \mu\text{m}$  spatial resolution, we reconstruct the complete 3D spatiotemporal intensity distribution (Ext. Data Fig. 3b).

To demonstrate the versatility and reconfigurability of RIPA, we characterize the asynchronous operation of independent optical spots. We report the reconstructed dynamics of two spots following a 1D zigzag trajectory (Ext. Data Fig. 3c) exhibiting a characteristic switching time of 200 ns.

These results, along with those in Fig. 4, are obtained using a tapered amplifier (TA) between the EOM and the second-order filter to boost input power into the RIPA. The observed dynamics thus reflect the RF response, the TA response, the APD response, and the round-trip propagation within the RIPAs. The fact that we could still observe fast dynamics is attributed to the intrinsic high bandwidth of the TA, alleviating EOM power-handling limitations. Numerical simulation of the RIPA pulsed rising response is shown in Ext. Data. Fig. 4c, revealing a quantitative agreement with the experimental result.

### 3. Properties of RIPA output

#### Electric field in the focal plane

The electric field in the RIPA focal plane is expressed as:

$$\begin{aligned} E_{\text{focal}}(k_x, k_y) &= \mathcal{F}[E_{\text{array}}(\mathbf{r})] \\ &= \mathcal{F} \left[ G(\mathbf{r}, w_0) \otimes \sum_{i=0, j=0}^{N_x-1, N_y-1} e^{i(i\varphi_x + j\varphi_y)} \delta(\mathbf{r} - p(i\mathbf{e}_x + j\mathbf{e}_y)) \right] \\ &= \mathcal{F}[G(\mathbf{r}, w_0)] \cdot e^{-i\phi_0} \\ &\quad \cdot \frac{\sin\left(\frac{N_x}{2}(k_x p - \varphi_x)\right)}{\sin\left(\frac{1}{2}(k_x p - \varphi_x)\right)} \cdot \frac{\sin\left(\frac{N_y}{2}(k_y p - \varphi_y)\right)}{\sin\left(\frac{1}{2}(k_y p - \varphi_y)\right)} \end{aligned} \quad (\text{S1})$$

where  $(i, j)$  index the beams,  $(N_x, N_y) = (8, 9)$  is the size of the beam array,  $p = 1\ \text{mm}$  is the lattice pitch dictated by the MLA, and  $G(\mathbf{r}, w_0)$  is the single-beam Gaussian profile with waist  $w_0$  at position  $\mathbf{r} = x\mathbf{e}_x + y\mathbf{e}_y$ .

Fourier transformation by the lens maps the field component at spatial frequency  $k_x, k_y$  to coordinate  $x_f = \frac{\lambda_f}{2\pi} k_x, y_f = \frac{\lambda_f}{2\pi} k_y$ , yielding the image-plane intensity:

$$\begin{aligned} |E_{\text{focal}}(x_f, y_f)|^2 \\ = \left| G\left(x_f, y_f, \frac{f\lambda}{\pi w_0}\right) \right|^2 \cdot \frac{\sin^2\left(N_x \pi \frac{x_f - x_0}{L}\right)}{\sin^2\left(\pi \frac{x_f - x_0}{L}\right)} \frac{\sin^2\left(N_y \pi \frac{y_f - y_0}{L}\right)}{\sin^2\left(\pi \frac{y_f - y_0}{L}\right)} \end{aligned} \quad (\text{S2})$$

Here  $L = \frac{f\lambda}{p}$  is the Brillouin zone extent, and  $(x_0, y_0) = (L \frac{\varphi_x}{2\pi}, L \frac{\varphi_y}{2\pi})$  defines the interference peak center. Equation. S2 reflects a standard grating distribution arising

from multi-beam interference, modulated by a Gaussian envelope  $\left|G\left(x_f, y_f, \frac{f\lambda}{\pi w_0}\right)\right|^2$  with waist  $w_f = \frac{f\lambda}{\pi w_0}$ , which is the Fourier transform of the common Gaussian mode (with waist  $w_0$ ) that each beam within the 2D phased array shares.

In the vicinity of the interference peak, the *grating function*  $g(x) \equiv \frac{\sin^2(N\pi x/L)}{\sin^2(\pi x/L)}$  approximates a Gaussian  $g(x) = N^2 \exp(-\alpha(\frac{x}{L})^2) + o(x^4)$ , where  $\alpha = \frac{\pi(N^2-1)}{3}$ . The equivalent Gaussian waist is  $w'_0 = L\sqrt{\frac{2}{\alpha}} = \frac{f\lambda}{\pi p} \sqrt{\frac{6}{N^2-1}}$ . As detailed in Supplementary Information, the deviation from this approximation is significant only beyond one waist  $w'_0$  away from the peak. Under typical operating conditions ( $p \gg w_0, N \gg 1$ ), the focal-plane intensity is *grating-limited*: peak width and spacing are governed by the pitch  $p$ , while the Gaussian envelope remains quasi-uniform across individual interference peaks.

#### Number of Brillouin zones and power concentration

The ratio between the MLA pitch  $p$  and the RIPA beam waist  $w_0$  determines the effective number of Brillouin zones  $M = w_{\text{env}}/L = p/(\pi w_0)$ . To minimize round-trip clipping losses at the MLA pupil, the RIPA typically operates in the  $p \gg w_0$  region, yielding  $M \gg 1$ . While this enables parallel spatial addressing over a  $\sim M \times M$  grid, it conversely suffers from the amplitude non-uniformity due to the slowly-varying Gaussian envelope and degraded interference quality due to the individual beam field curvature.

Optical power can be concentrated within the first Brillouin zone by increasing  $w_0$  relative to  $p$  using a MLA-telescope (focal lengths  $f_1, f_2$ ; separation  $d = f_1 + f_2$ ) at the array output, effectively forming a local telescope for each individual beam. The resulting magnification increase clipping loss which remains acceptable as there is only a single pass.

#### Off-focal intensity distribution

Numerical simulations confirm that the intensity distribution beyond the focal plane approximates a Gaussian beam (Fig. 4d,f). This behavior can be understood intuitively by treating the 2D phased array as a “distributed” large beam with a tilted wavefront and a quasi-continuous amplitude profile. Simulations at discrete frequencies demonstrate that changing the phase difference  $\varphi_x$  shifts the beam “waist” along the  $x$  direction, while the  $z$ -position remains fixed. The intensity asymmetry along the  $x$  axis in Fig. 4d,f results from monotonic power decay due to round-trip losses.

### Trajectory stabilization with MLA against the imperfections of the optics

In the absence of the MLA, the round trips are susceptible to imperfections such as mirror curvature, aberrations, astigmatism, and surface roughness. These can be modeled as a low-spatial-frequency (“DC”) noise acting on the circulating beam. In the ray limit characterized by position  $x$  and momentum  $\theta_x$ , this noise imparts near-constant “momentum kicks” that accumulate after multiple round trips. The MLA introduces a “cavity-like”, or lensguide, confinement that effectively “traps” the light, rendering the dynamics insensitive to “DC” noise, as momentum kicks sum out-of-phase and largely cancel. Similarly, the ray dynamics is insensitive to other low-frequency noise up to the “trap frequency”  $\theta_{\text{gouy}}/(2\pi p)$ .

Formally, following Ref. [60], the ray can be viewed as evolving under an adiabatically time-varying Hamiltonian induced by optical imperfections. Rays initialized in an eigenstate of this Hamiltonian remain an eigenstate under this adiabatic evolution due to the finite energy gap arising from the MLA’s transversal confinement. In contrast, without the MLA, the 4f system is degenerate for all beams and lacks this stabilization property.

### Tolerance to misalignment

System misalignment, stemming from mode mismatch or optical aberrations, is analyzed by decomposing each beam into the local Hermite-Gaussian basis  $|lm\rangle = \text{TEM}_{lm}$  on each microlens. In an ideal case, all beams share the fundamental Gaussian mode  $|00\rangle$ . Tilt or positional misalignments primarily excite the lowest-order odd modes  $|10\rangle$  or  $|01\rangle$ , while a mode-size mismatch primarily excites even modes such as  $|20\rangle$ . Because these modes possess distinct Gouy phases  $\psi(z) = (l + m + 1) \arctan\left(\frac{z}{z_R}\right)$ , they focus at different transverse positions relative to the  $|00\rangle$  mode in the focal plane.

Owing to their parity, the  $|10\rangle$  or  $|01\rangle$  modes exhibit vanishing intensity at the center of the Brillouin zone. To quantify this suppression, we integrate the field intensity over the first Brillouin zone, defining the suppression factor  $S = \frac{\int_{\text{1st Brillouin zone}} |E_{00}|^2 dx_f dy_f}{\int_{\text{1st Brillouin zone}} |E_{01}|^2 dx_f dy_f}$ . In our system with a Gouy phase per round trip of  $\pi/2$ , and the suppression  $S$  ranges between 10.7 and 249 at different places within the Brillouin zone, with an average value of 66.4.

### Lensing effect compared with AOD

We evaluate the RIPA-equivalent acoustic lensing effect as in AODs [34, 35]. By calculating the focal shift  $\delta z$  induced by frequency chirping in both RIPA and AOD, we derive the ratio (See the Supplementary Information

Ext. Data Table I. **Power efficiency analysis of the RIPA.** Internal loss per round trip comprises absorption, clipping, and scattering into higher-order modes.

Quantity	Symbol	Value (%)
1 <sup>st</sup> RIPA round-trip loss	$A_1 = \kappa_1 + l_1$	5.1(9)
- Out-coupling	$\kappa_1$	2.9(7)
- Internal loss	$l_1$	2.2(1.1)
1 <sup>st</sup> RIPA efficiency	$\eta_1 = \kappa_1 \cdot \sum_{j=0}^{N_y-1} (1 - A_1)^j$	21.9(2)
Relay system efficiency	$\eta_{\text{rel}}$	70.6(4)
2 <sup>nd</sup> RIPA round-trip loss	$A_2 = \kappa_{2,\text{lock}} + \kappa_2 + l_2$	19.8(1.8)
- Locking path	$\kappa_{2,\text{lock}}$	9.7(9)
- Out-coupling	$\kappa_2$	6.8(7)
- Internal loss	$l_2$	3.3(2.2)
2 <sup>nd</sup> RIPA efficiency	$\eta_2 = \kappa_2 \cdot \sum_{i=0}^{N_x-1} (1 - A_2)^i$	28.3(5)
SLM + imaging efficiency	$\eta_{\text{im}}$	85(5)
<b>Total system efficiency</b>	$\eta = \eta_1 \cdot \eta_{\text{rel}} \cdot \eta_2 \cdot \eta_{\text{im}}$	<b>3.7(1)</b>

for a detailed derivation):

$$\left| \frac{\delta z_{\text{RIPA}}}{\delta z_{\text{AOD}}} \right| = \frac{1}{\sqrt{6}} \frac{\tau_{\text{RIPA}}}{\tau_{\text{AOD}}} \quad (\text{S3})$$

under identical sweeping speeds and focal waist size  $w_0'$  in the focal plane. Here  $\tau_{\text{RIPA}} = \frac{NL_{\text{rt}}}{c}$  and  $\tau_{\text{AOD}} = \frac{w_0}{v_s}$  denote the characteristic propagation times in RIPA and AOD, respectively. Consequently, our current device exhibits a suppressed lensing effect (0.027 $\times$ ) relative to an AOD with a  $\tau_{\text{AOD}} \sim 1 \mu\text{s}$  switching time. Numerical simulation result presented in Ext. Data. Fig. 4e shows the lensing trajectory under linear frequency chirping of various durations ( $T = 200, 500$ , and  $2000 \text{ ns}$ ), confirming the fast and continuous steering of the addressing beam with tolerable lensing effect.

## 4. Scaling up the RIPA

### Power efficiency and loss budget

Analysis of power efficiencies are detailed in Ext. Data Table 4. The round-trip losses  $A_1$  and  $A_2$  are extracted by fitting the intensity distribution of the output 2D beam array to an exponential decay model. These losses comprise out-coupling and internal losses; notably, the second stage incorporates a locking-path beamsplitter ( $\kappa_{2,\text{lock}}$ ) that introduces additional loss. The measured total system efficiency of 3.7(1)% is primarily limited by the out-coupling ratio (see discussion in the following section).

The fundamental scalability of the RIPA is governed by internal losses (if the internal loss is high, the beams cannot make many round trips in the RIPA). Transitioning to a standing-wave two-mirror configuration would eliminate the locking path, substantially reducing intrinsic losses. Currently, round-trip loss is 2–3%, comprising mirror losses ( $\sim 1\%$ , 1X Thorlabs BB1-EO3, 3X

Thorlabs UM10-45A), lens surface reflections ( $\sim 1\%$ , 8X V-coated surfaces), and MLA reflections ( $\sim 1\%$ , Edmund Optics #21-155). Replacing the MLA with a high-reflectivity micro-mirror array (MMA) further reduce the surface reflection loss. We calculate the clipping loss at the MLA to be  $\exp\left(-\frac{2(d/2)^2}{(\sqrt{2}w_0)^2}\right) = 0.005\%$  which is negligible, where  $d = 500 \mu\text{m}$  is the MLA pupil size. However, due to imperfect mode-matching or aberration-induced oscillations, the higher-order modes may experience higher clipping loss at the MLA.

To conclude, adopting a two-mirror geometry, MMAs, and nano-textured optics should reduce round-trip loss to  $< 1\%$ . This improvement would support hundreds of round trips, enabling  $100 \times 100$  beam arrays in the near term.

#### Footprint scaling

The system footprint is primarily determined by the round-trip length of the second RIPA. To maintain a similar modulation bandwidth (i.e. frequency resolution of the second RIPA  $f_{\text{res}} = c/(N_x L_{\text{r,t2}}) \sim \text{MHz}$ ), the second RIPA round-length of a scaled-up device will be, actually, *shorter* than the current design. This arises because light circulates  $N_x$  times within the second RIPA. Under scaling, the attainable EOM aggregation bandwidth (tens of GHz) becomes the primary constraint rather than the physical footprint. Numerical analysis indicates that a  $100 \times 100$  RIPA SLM with 1 MHz per-pixel bandwidth operates at a sweet point, with an aggregation bandwidth of 10 GHz and a meter-scale footprint of  $L_{\text{r,t2}} \sim 1.5 \text{ m}$ .

#### Tradeoff between power efficiency and linewidth

Increasing the power out-coupling ratio per round trip improves the RIPA system's power efficiency. However, the resulting intensity decay in successive round trips degrades the interference pattern by reducing the effective number of interfering beams, thereby broadening the linewidth. This establishes an inherent tradeoff between power efficiency and interference linewidth. We numerically simulate the  $1/e^2$  waist ( $w$ ) of the interference peak as a function of power out-coupling ratio ( $\kappa$ ) with a certain internal loss ( $l$ ). We define the linewidth broadening factor  $R_w \equiv w/\lim_{\kappa \rightarrow 0, l \rightarrow 0} w$  as the ratio of  $w$  to the diffraction-limited waist attained when all output beams have uniform intensity.

Ext. Data Fig. 5 illustrates this tradeoff for the first ( $N_y = 9$ , internal loss  $l_1 = 2.2\%$ ), the second RIPA ( $N_x = 8$ , internal loss  $l_2 + \kappa_{2,\text{lock}} = 13\%$ ), and the proposed  $100 \times 100$  RIPA ( $N_x = N_y = 100$ , internal loss  $l_{100} = 1\%$ ). Experimentally, we operate at  $\kappa_1 = 2.9\%$  and  $\kappa_2 = 6.8\%$  (gray dashed lines). Depending on the application, the system can be optimized for either power efficiency or interference quality. This tradeoff is remark-

ably favorable: with sufficiently low internal loss, one can utilize  $> 80\%$  power without significantly interference pattern degradation ( $< 10\%$  linewidth increase).

#### 5. Lens-guide mode waist and stability region

##### “Half confocal” lens-guide mode

The round-trip dynamics of a beam within the RIPA lens-guide comprises propagation over a distance  $L_{\text{rt}}/2$ , a lens with focal length  $f$ , and another propagation over  $L_{\text{rt}}/2$ . In terms of the ABCD Matrix, we have

$$\begin{aligned} M &= \begin{pmatrix} 1 & L_{\text{rt}}/2 \\ 0 & 1 \end{pmatrix} \begin{pmatrix} 1 & 0 \\ -\frac{1}{f} & 1 \end{pmatrix} \begin{pmatrix} 1 & L_{\text{rt}}/2 \\ 0 & 1 \end{pmatrix} \\ &= \begin{pmatrix} 1 - \frac{L_{\text{rt}}}{2f} & L_{\text{rt}} - \frac{L_{\text{rt}}^2}{4f} \\ -\frac{1}{f} & 1 - \frac{L_{\text{rt}}}{2f} \end{pmatrix} \equiv \begin{pmatrix} A & B \\ C & D \end{pmatrix}. \end{aligned} \quad (\text{S4})$$

The eigenmode Gaussian parameter  $q_e$  satisfies  $q_e = (Aq_e + B)/(Cq_e + D)$ , which yields the solution  $q_e = i\sqrt{L_{\text{rt}}(f - L_{\text{rt}}/4)}$ . The resulting mode waist is  $w_0 = \sqrt{\lambda \text{Im}(q)/\pi}$ . To achieve the maximum alignment stability against mode-mismatch, we operate at  $L_{\text{rt}} = 2f$  and  $w_0 = \sqrt{f\lambda/\pi}$ . This configuration corresponds to a Gouy phase  $\phi_{\text{gouy}} = 2 \arctan(L_{\text{rt}}/2/\text{Im}(q)) = 2 \arctan(1) = \pi/2$ , which is exactly half of the Gouy phase obtained in a confocal cavity. We denote this the “half confocal” regime. Operating in this regime guarantees maximal mode overlap across the 2D phased array in the presence of input mode mismatch or aberration-induced distortions, maintaining high-quality interference. Additionally, this condition minimizes the spot size on the MLA pupil ( $w_{\text{MLA}} = \sqrt{2}w_0 = \sqrt{2\lambda f/\pi}$ ), thereby minimizing the clipping loss.

#### Ray tracing simulations

Ray tracing simulations (Fig. 1b) were performed using an in-house, open-source package [56] for non-paraxial propagation through spherical, aspheric, and microlens array optics. The software's GUI enables real-time manipulation of experimental variables, providing critical insights for optical alignment.

To simulate the 2D beam array interference pattern at the focal plane, we utilized an in-house, open-source wave propagation package [57]. This allows for wave-optics analysis accounting for misalignment, phase errors, and time-dependent driving sequences.